time-of-flight secondary ion mass spectrometry (ToF-SIMS) (fig. S11F) (*19*) and found higher Cl content in $CH_3NH_3PbI_3(Cl)$ films than in $CH_3NH_3PbI_3$ films without Cl. This technique probes the top 2 nm of the film.

Although perovskite solar cells have better radiative efficiencies than many other types, such as dye-sensitized, organic, or even cadmium telluride solar cells, they still suffer from greater nonradiative losses than inorganic materials such as gallium arsenide and are only at present approaching the radiative efficiencies of copper indium gallium selenide (CIGS) (*31*). Our results identify a subpopulation of dark grains and grain boundaries as specific targets for perovskite growth and passivation studies, and show that local fluorescence lifetime imaging provides a route by which changes in film processing can be evaluated to assess their influence on carrier recombination in films. By removing these nonradiative pathways to obtain uniform brightness with high emissivity across all grains, it is likely that we will see the performance of perovskite devices approach the thermodynamic limits for solar cells and other light-emitting devices.

REFERENCES AND NOTES

1. T. C. Sum, N. Mathews, *Energ. Environ. Sci.* **7**, 2518–2534 (2014).
2. M. A. Green, A. Ho-Baillie, H. J. Snaith, *Nat. Photonics* **8**, 506–514 (2014).
3. J. Burschka *et al.*, *Nature* **499**, 316–319 (2013).
4. G. E. Eperon, V. M. Burlakov, P. Docampo, A. Goriely, H. J. Snaith, *Adv. Funct. Mater.* **24**, 151–157 (2014).
5. G. Xing *et al.*, *Nat. Mater.* **13**, 476–480 (2014).
6. G. E. Eperon *et al.*, *Energ. Environ. Sci.* **7**, 982–988 (2014).
7. J. H. Noh, S. H. Im, J. H. Heo, T. N. Mandal, S. I. Seok, *Nano Lett.* **13**, 1764–1769 (2013).
8. National Center for Photovoltaics at the National Renewable Energy Laboratory, Research cell efficiency records, www.nrel.gov/ncpv/ (accessed 11 April 2015).
9. S. D. Stranks *et al.*, *Science* **342**, 341–344 (2013).
10. H. Zhou *et al.*, *Science* **345**, 542–546 (2014).
11. O. D. Miller, E. Yablonovitch, S. R. Kurtz, *IEEE J. Photovolt.* **2**, 303–311 (2012).
12. N. K. Noel *et al.*, *ACS Nano* **8**, 9815–9821 (2014).
13. J. You *et al.*, *ACS Nano* **8**, 1674–1680 (2014).
14. P. W. Liang *et al.*, *Adv. Mater.* **26**, 3748–3754 (2014).
15. S. D. Stranks *et al.*, *Phys. Rev. Appl.* **2**, 034007 (2014).
16. F. Deschler *et al.*, *J. Phys. Chem. Lett.* **5**, 1421–1426 (2014).
17. C. Wehrenfennig, M. Liu, H. J. Snaith, M. B. Johnston, L. M. Herz, *Energ. Environ. Sci.* **7**, 2269–2275 (2014).
18. J. S. Manser, P. V. Kamat, *Nat. Photonics* **8**, 737–743 (2014).
19. See the supplementary materials on *Science* Online.
20. G. Xing *et al.*, *Science* **342**, 344–347 (2013).
21. Y. Yamada, T. Nakamura, M. Endo, A. Wakamiya, Y. Kanemitsu, *J. Am. Chem. Soc.* **136**, 11610–11613 (2014).
22. M. Saba *et al.*, *Nat. Commun.* **5**, 5049 (2014).
23. A. Abate *et al.*, *Nano Lett.* **14**, 3247–3254 (2014).
24. S. Watanabe *et al.*, *Nat. Methods* **8**, 80–84 (2011).
25. E. Edri *et al.*, *Nano Lett.* **14**, 1000–1004 (2014).
26. W. J. Yin, T. Shi, Y. Yan, *Adv. Mater.* **26**, 4653–4658 (2014).
27. M. M. Lee, J. Teuscher, T. Miyasaka, T. N. Murakami, H. J. Snaith, *Science* **338**, 643–647 (2012).
28. P. Gao, M. Grätzel, M. K. Nazeeruddin, *Energ. Environ. Sci.* **7**, 2448–2463 (2014).
29. K. Munechika *et al.*, *Nano Lett.* **11**, 2725–2730 (2011).
30. X. Wen *et al.*, *J. Phys. Chem. Lett.* **5**, 3849–3853 (2014).
31. K. Tvingstedt *et al.*, *Sci. Rep.* **4**, 6071 (2014).
32. S. De Wolf *et al.*, *J. Phys. Chem. Lett.* **5**, 1035–1039 (2014).
33. C. H. Seager, *Annu. Rev. Mater. Sci.* **15**, 271–302 (1985).
34. J. S. Yun *et al.*, *J. Phys. Chem. Lett.* **6**, 875–880 (2015).
35. Q. Dong *et al.*, *Science* **347**, 967–970 (2015).
36. W. Nie *et al.*, *Science* **347**, 522–525 (2015).
37. D. Shi *et al.*, *Science* **347**, 519–522 (2015).
38. M. Grätzel, *Nat. Mater.* **13**, 838–842 (2014).
39. G. Grancini *et al.*, *J. Phys. Chem. Lett.* **5**, 3836–3842 (2014).
40. Y. Tidhar *et al.*, *J. Am. Chem. Soc.* **136**, 13249–13256 (2014).
41. S. T. Williams *et al.*, *ACS Nano* **8**, 10640–10654 (2014).

ACKNOWLEDGMENTS

This material is based in part on work supported by the State of Washington through the University of Washington Clean Energy Institute. D.W.D. acknowledges support from an NSF Graduate Research Fellowship (DGE-1256082). S.M.V. acknowledges support from a National Defense Science and Engineering Graduate Fellowship. The research leading to these results has received funding from the European Union Seventh Framework Program (FP7/2007-2013) under Grant Agreement No. 604032 of the MESO project. G.E.E. is supported by the Engineering and Physical Sciences Research Council and Oxford Photovoltaics through a Nanotechnology Knowledge Transfer Network Collaborative Award in Science and Engineering. The authors gratefully acknowledge funding from the National Institute for Biomedical Imaging and Bioengineering (NIH grant EB-002027) supporting the National ESCA and Surface Analysis Center for Biomedical Problems and ToF-SIMS instrumentation. D.W.D. thanks I. Braly, S. Braswell, D. Moerman, and B. Miller for valuable assistance. S.M.V. gratefully acknowledges D. Graham for assistance with ToF-SIMS. Additional data, including materials, methods, and key controls, are available online as supplementary materials (*19*).

SUPPLEMENTARY MATERIALS

www.sciencemag.org/content/348/6235/683/suppl/DC1
Materials and Methods
Supplementary Text
Figs. S1 to S11

19 December 2014; accepted 14 April 2015
10.1126/science.aaa5333

CATALYSIS

Identification of molybdenum oxide nanostructures on zeolites for natural gas conversion

Jie Gao,[1] Yiteng Zheng,[1] Jih-Mirn Jehng,[2,3] Yadan Tang,[2]
Israel E. Wachs,[2]* Simon G. Podkolzin[1]*

Direct methane conversion into aromatic hydrocarbons over catalysts with molybdenum (Mo) nanostructures supported on shape-selective zeolites is a promising technology for natural gas liquefaction. We determined the identity and anchoring sites of the initial Mo structures in such catalysts as isolated oxide species with a single Mo atom on aluminum sites in the zeolite framework and on silicon sites on the zeolite external surface. During the reaction, the initial isolated Mo oxide species agglomerate and convert into carbided Mo nanoparticles. This process is reversible, and the initial isolated Mo oxide species can be restored by a treatment with gas-phase oxygen. Furthermore, the distribution of the Mo nanostructures can be controlled and catalytic performance can be fully restored, even enhanced, by adjusting the oxygen treatment.

Methane (CH_4), the main component of natural gas, has the highest H-to-C ratio of all hydrocarbons; therefore, it is more environmentally friendly in terms of CO_2 emissions than oil or coal-derived fuels. However, 30 to 60% of natural gas reserves are classified as "stranded" because shipping gas is not economical, and the costs of liquefaction or building a pipeline are usually prohibitively high (*1*–*5*). The problem of natural gas utilization is exacerbated by burning and venting of the associated gas produced in the course of crude oil production at remote locations. Conversion of methane into shippable liquids can solve these problems but remains scientifically challenging (*1*–*3*, *6*–*8*).

One of the technologies under development is direct methane conversion into liquid aromatic hydrocarbons in a single step (dehydroaromatization with the main reaction $6CH_4 \rightarrow C_6H_6 + 9H_2$) using catalysts with Mo nanostructures supported on shape-selective zeolites (*2*, *8*–*16*). This technology offers two advantages over other methane activation chemistries: Complete oxidation, as well as explosive combustion, is not possible because of the absence of O_2 or other oxidizing reagents, and processing can be performed at remote locations because no reagents are needed. The biggest issues in commercialization are rapid catalyst deactivation and comparatively low single-pass conversion levels of ~10% (*2*, *8*, *13*–*16*). Development of improved catalysts has been hindered by a lack of molecular-level understanding of the identity of the zeolite-supported Mo nanostructures and their structural transformations.

We studied Mo nanostructures supported on ZSM-5 zeolites by combining quantum chemical calculations using density functional theory (DFT) with multiple spectroscopic techniques, including in situ ultraviolet-visible diffuse reflectance

---

[1] Department of Chemical Engineering and Materials Science, Stevens Institute of Technology, Hoboken, NJ 07030, USA. [2] Operando Molecular Spectroscopy and Catalysis Laboratory, Department of Chemical Engineering, Lehigh University, Bethlehem, PA 18015, USA. [3] Department of Chemical Engineering, National Chung Hsing University, Taichung, Taiwan, Republic of China.
***Corresponding author. E-mail: iew0@lehigh.edu (I.E.W.); simon.podkolzin@stevens.edu (S.G.P.)**

Downloaded from www.sciencemag.org on August 30, 2015

spectroscopy (UV-vis DRS), in situ infrared (IR) spectroscopy, and operando Raman spectroscopy at elevated reaction temperatures with simultaneous online mass spectrometry of reaction products. We determined the identity and anchoring sites of the initial Mo oxide nanostructures and established structure-activity relationships. The catalytic activity can be fully restored by regenerating initial Mo oxide nanostructures with a gas-phase O_2 treatment. Furthermore, the activity can even be enhanced by controlling the distribution of Mo oxide nanostructures by adjusting conditions of such an O_2 regeneration treatment.

Molybdenum nanostructures supported on zeolites were initially present in an oxide form after Mo deposition and an oxygen treatment at elevated temperatures (our samples were calcined at 773 K) (*17*). The number of MoO_x units in an average individual nanostructure was evaluated using the edge energy (E_g) of the in situ UV-vis DRS spectra. The E_g values for the following well-defined Mo oxide reference compounds are presented in Fig. 1A: (i) MoO_6-coordinated Mo_7-Mo_{12} clusters, (ii) linear chains of alternating MoO_4 and MoO_6 units, (iii) infinite layered sheets of MoO_5 units, (iv) Mo_2O_7 dimer as MoO_3-O-MoO_3, (v) isolated MoO_4 and MoO_6 monomers, and (vi) aqueous molybdate anions as a function of the solution pH (*18*). The E_g values in Fig. 1A exhibit a linear correlation with the number of bridging Mo-O-Mo covalent bonds around the central Mo cation and, correspondingly, with the number of MoO_x units in a nanostructure. The E_g value for a representative catalyst sample with 2 weight percent (wt %) Mo supported on a ZSM-5 (Si/Al = 15) zeolite, which is the most common zeolite evaluated for methane dehydroaromatization, was 4.8 eV, which falls in the range of isolated MoO_x nanostructures with a single Mo atom.

The nature of the Mo oxide nanostructures was further examined with in situ Raman spectroscopy by varying the concentration of Mo from 0.7 to 3.3 wt % on a ZSM-5 zeolite support with a constant Si/Al ratio of 15 (Fig. 1B) and by varying the Si/Al ratio from 15 to 140 at a constant Mo concentration of 1.3 wt % (Fig. 1C). The spectrum for 1.3 wt % Mo on ZSM-5 with Si/Al = 15 is shown in both sets in Fig. 1, B and C, and a similar spectrum is shown in operando Raman measurements with methane flow in fig. S1 (*17*). The absence of sharp Raman bands from crystalline MoO_3 nanoparticles (NPs) at 996, 815, and 666 cm^{-1} (*19*) or crystalline $Al_2(MoO_4)_3$ at ~1004 and 1045 cm^{-1} (*18*, *20*) indicates, in agreement with the UV-vis results in Fig. 1A, that Mo oxide was completely dispersed; any amorphous Mo oxide species would crystallize at the elevated pretreatment temperature of 773 K. Some spectra exhibited weak shoulder features at 950 cm^{-1} from Mo oxide species in zeolite framework vacancy defects and at 1026 cm^{-1} from Mo oxide species on extra-framework alumina NPs (*17*).

For the ZSM-5 (Si/Al = 15) zeolite in Fig. 1B, a single Raman band at 993 cm^{-1} was observed in the Mo-O stretching region for all Mo concentrations. However, at higher Si/Al ratios in Fig. 1C, a new band at 975 cm^{-1} was observed, and an additional band appeared at 984 cm^{-1} at the highest Si/Al = 140 (Fig. 1C). These three bands cannot be attributed to a single Mo oxide nanostructure because their relative intensities change with the Si/Al ratio. To determine the identity and anchoring sites of these Mo oxide structures in the ZSM-5 zeolite framework, various monomeric Mo oxide species were evaluated with DFT calculations, and the calculated normal vibrational modes were compared with the experimental Raman spectra.

After calcination at 773 K, Mo was present in its highest oxidation state of +6, as evidenced by the absence of d-d transitions for reduced Mo in the in situ UV-vis spectra. Our DFT calculations show that neutral MoO_3 species on framework Si sites are unstable and that framework Al sites are required for anchoring (*17*). This result is in agreement with changes in the in situ IR spectra for surface OH groups as a function of the Mo loading in fig. S2 (*17*) that showed preferential elimination of Brønsted acid sites (H^+ on $[AlO_4]^-$) after Mo deposition. On a site with two adjacent framework Al atoms, the stoichiometry of the Mo oxide species should be $Mo(=O)_2^{2+}$ as dioxo species to counterbalance the 2– charge of $2[AlO_4]^-$ and maintain Mo in the +6 oxidation state. The size of isolated Mo dioxo species serves as a geometric restriction, which determines the acceptable range of separation distances between the two anchoring framework Al-atom sites. Because ZSM-5 is a Si-rich zeolite, Lowenstein's rule prohibits one Al atom to be the first neighbor of another Al atom in the framework as Al-O-Al. An arrangement of Al-O-Si-O-Al with two Al atoms as second neighbors was not found experimentally, based on ^{27}Al nuclear magnetic resonance (NMR) and additional characterization for ZSM-5 samples with Si/Al > 8 (*21*, *22*). Finally, an arrangement of Al-O-$(Si-O)_2$-Al with two Al atoms as third neighbors must be the only possible double Al-atom anchoring sites for Mo dioxo species. Our DFT results confirm that two Al atoms as fourth neighbors in Al-O-$(Si-O)_3$-Al can serve only as two individual single anchoring sites (*17*).

Although the exact distribution of Al atoms among different framework sites in ZSM-5 zeolites is currently not well understood, it can be varied by adjusting the zeolite synthesis procedure. For example, the number of Al atoms as double anchoring sites in the arrangement Al-O-$(Si-O)_2$-Al can be varied from 4 to 46% for ZSM-5 samples with Si/Al = ~20, based on characterization with hydrated Co cations (*22*). The fraction of Al atoms as double anchoring sites typically decreases, but not proportionally, with the increasing Si/Al ratio for the same synthesis procedure (*22*). Our evaluation of Al-O-$(Si-O)_2$-Al arrangements in ZSM-5 shows that these sites can serve as double Al-atom anchoring sites if they are located in the same channel, but not in the same plane. Additional classification of double Al-atom anchoring sites is provided in fig. S4 (*17*). A representative $Mo(=O)_2^{2+}$ dioxo structure on

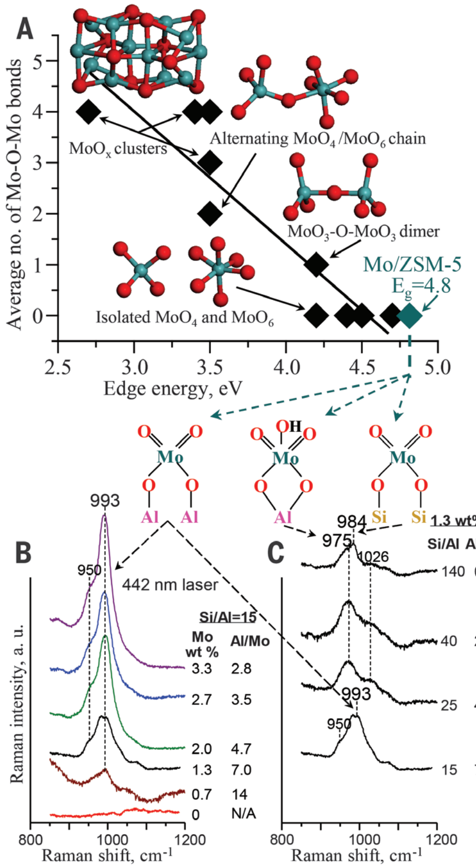

Fig. 1. Spectroscopic measurements. (**A**) Electronic edge values based on in situ UV-vis spectra of reference Mo oxide compounds exhibit a linear correlation with the number of bridging Mo-O-Mo covalent bonds around the central Mo cation. The value of 4.8 eV for 2 wt % Mo/ZSM-5 (Si/Al = 15) corresponds to Mo oxide species with a single Mo atom. (**B** and **C**) In situ Raman spectra of Mo/ZSM-5 catalysts under oxygen flow at 773 K as a function of (B) Mo loading for constant Si/Al = 15 and (C) Si/Al ratio for constant 1.3 wt % Mo loading with band assignments to Mo oxide species based on DFT calculations. a. u., arbitrary units.

an anchoring site with a pair of Al atoms in T8 and T12 framework positions is shown in Fig. 2. In this nanostructure, the Mo atom is bridge-bonded to two framework Al atoms through two neighboring framework oxygen atoms and terminated with two additional oxygen atoms. The normal vibrational modes obtained with DFT calculations for these terminal oxygen atoms in $Mo(=O)_2^{2+}$ are summarized in Table 1. The symmetric stretch (ν_s) is calculated to be at 992 cm^{-1}. The calculated geometries and normal vibrational modes for the $Mo(=O)_2^{2+}$ nanostructure on other double Al-atom anchoring sites with two bridging framework O atoms are similar (table S2 and fig. S6) (*17*). On a site with a single framework Al atom, the stoichiometry of Mo oxide species should be $Mo(=O)_2(OH)^+$ to counterbalance the 1– charge of $[AlO_4]^-$ and maintain Mo in the +6 oxidation state. The vibrational mode for the symmetric stretch of the terminal oxygen atoms in these Mo species is predicted to be at 975 cm^{-1}, based on evaluation of geometries and vibrational modes of the $Mo(=O)_2(OH)^+$ nanostructure anchored on single Al-atom sites in T8 (Table 1) and other ZSM-5 framework positions (table S1 and fig. S5) (*17*).

Raman spectroscopy gives rise to strong bands of symmetric stretches (ν_s) and weaker bands of asymmetric stretches (ν_{as}), with the latter sometimes being undetectable. In our previous studies of MoO_3/SiO_2 (*19*, *20*), ν_{as} for $Mo(=O)_2$ was not observed for Mo loadings below 4 wt %. Therefore, only ν_s is expected to be observed for lower Mo loadings. A comparison of the dominant Raman bands at 975 and 993 cm^{-1} in Fig. 1 with the calculated symmetric stretch values (ν_s) in Table 1 (975 and 992 cm^{-1}) allowed us to assign these bands to two distinct isolated Mo dioxo species anchored on, respectively, single and double Al-atom framework sites.

The identification of the isolated Mo oxide structures provided insight as to how they were affected by the main catalyst formulation parameters: the Mo loading and Si/Al ratio. At a low Si/Al = 15, Mo oxide species preferentially anchored on sites with two Al atoms (band at 993 cm^{-1} in Fig. 1B). Even at the highest Mo loading of 3.3 wt %, the Al/Mo atomic ratio is 2.8, which allowed all Mo atoms to be anchored on double Al-atom sites. However, when the Si/Al ratio increased, the number of Al atoms per unit volume of the zeolite decreased, and the number of sites with two Al atoms should have decreased more rapidly than the overall number of Al atoms. As a result, at higher Si/Al ratios of 25 and 40 in Fig. 1C, the dominant band was at 975 cm^{-1}, arising from $Mo(=O)_2OH$ species anchored on sites with one Al atom. The identification of single and double Al-atom anchoring sites is in agreement with previous findings that each Mo atom displaces one H^+ from framework $[AlO_4]^-$ sites in ZSM-5 with Si/Al = 40 and two H^+ in ZSM-5 with Si/Al = 15 (*23*). At the highest Si/Al = 140 shown in Fig. 1C, when the corresponding Al/Mo ratio fell below unity to 0.8, there were not even enough single Al-atom sites for stabilizing all Mo atoms. For this catalyst formulation, Mo oxide species were forced to be stabilized, not in the zeolite pores but on the least preferable Si sites on the external surface of the zeolite. A new band at 984 cm^{-1} for Si/Al = 140 in Fig. 1C is consistent with our previous Raman spectra for Mo oxide species supported on amorphous SiO_2 (*19*, *20*). Our DFT calculations confirmed that Mo dioxo species did not stabilize in zeolite pores in the absence of Al sites and that the structure of isolated $Mo(=O)_2$ dioxo species as $(Si\text{-}O\text{-})_2Mo(=O)_2$ on the external surface of the zeolite (Fig. 1; full details in fig. S8 and table S4) (*17*) is similar to that on SiO_2. These findings are also supported by the in situ IR spectra of the surface OH region for ZSM-5 (Si/Al = 15) as a function of the Mo loading in fig. S2 (*17*). The intensity of the peak at 3608 cm^{-1} for OH groups on framework Al sites (*24*) decreased through replacement by Mo oxide species at low Mo loadings, followed by a decrease in the intensity of the peak at 3745 cm^{-1} for OH groups on the external surface Si sites (*24*) at higher Mo loadings. The isolated Mo oxide structures preferentially anchored on double Al-atom framework sites, then single Al-atom framework sites, and finally Si sites on the external surface of the zeolite. The isolated Mo oxide nanostructures anchored on these three types of zeolite sites are shown schematically in Fig. 1 and with 3D animation in movie S1.

Dynamic changes of Mo nanostructures under reaction and regeneration conditions were evaluated by simultaneously collecting operando Raman spectroscopy and online mass spectrometry measurements, first with CH_4 flow at 953 to 1053 K (fig. S1) (*17*) and then under regeneration conditions with gas-phase O_2 flow at 773 K (figs. S10 and S11) (*17*). Upon CH_4 introduction, CO_2 was the only initial carbon-containing product, and the Raman band at 993 cm^{-1} for the isolated Mo oxide structures gradually disappeared. Because CH_4 was the only reactant, Mo oxide nanostructures reduced to oxycarbide or carbide species. Several studies with different techniques, such as x-ray absorption fine structure, Mo L_{III} edge x-ray absorption near-edge structure, and ^{95}Mo NMR, provide direct evidence that the reduced Mo phase is a carbide with the stoichiometry of MoC_x or MoC_xO_y and that the initial oxide species agglomerate into particles with a size of ~0.6 nm (*25*–*28*). After the induction period, CO_2 formation stopped, the Raman band at 993 cm^{-1} for the initial Mo oxide species was no longer observed (Fig. 2B and fig. S1) (*17*), and the catalyst performed CH_4 dehydroaromatization with C_6H_6 as the main hydrocarbon product.

Our results demonstrate that an O_2 treatment can reverse both the carbide formation and the agglomeration of Mo nanostructures. The Raman spectra at 753 K for the initial catalyst with isolated Mo oxide structures and for the regenerated catalyst after reaction in Fig. 2 are similar, with a single band at 993 cm^{-1} and a shoulder feature at 950 cm^{-1}. The similarity in the Raman band positions and intensities before reaction and after regeneration indicates that the regeneration converts carbided Mo NPs into an oxide phase, redisperses this phase into isolated oxide nanostructures with a single Mo atom, and allows these Mo oxide species to diffuse and then stabilize on substantially the same zeolite anchoring sites as in the initial catalyst before the reaction.

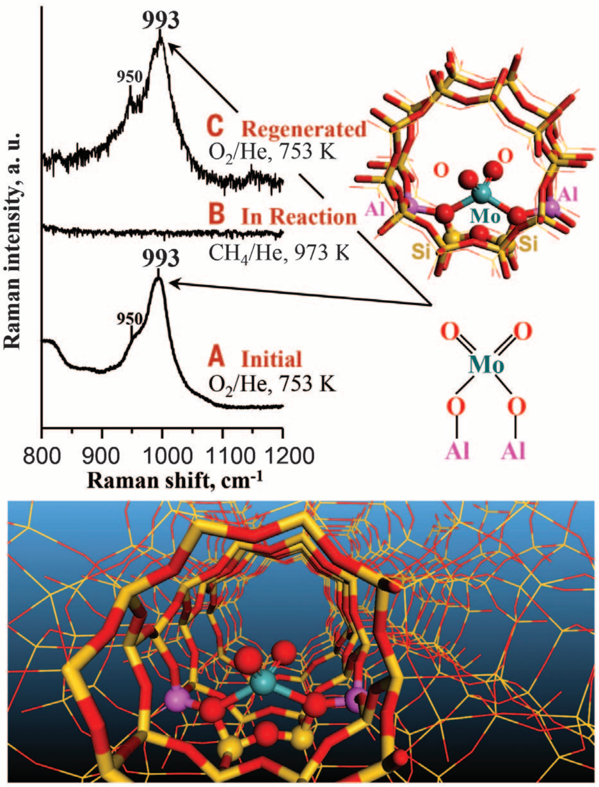

Fig. 2. Operando Raman spectra of 2 wt % Mo/ZSM-5 (Si/Al = 15). Spectra (**A**) after initial pretreatment with gas-phase oxygen, (**B**) during reaction with methane, and (**C**) after regeneration with gas-phase oxygen are shown. The spectra demonstrate that the initial $Mo(=O)_2^{2+}$ nanostructures anchored on double Al-atom framework sites (shown schematically on the right and in a zeolite pore below) with a vibrational mode at 993 cm^{-1} are recovered after regeneration.

Effects of regeneration time with O_2 on the identity of Mo nanostructures and on catalytic performance with CH_4 after regeneration were evaluated by combining additional Raman spectroscopic measurements with reaction testing. Raman spectra were collected in O_2 flow at 773 K for two 1.3 wt % Mo/ZSM-5 (Si/Al = 15 and 25) catalysts after their deactivation in reaction with CH_4. The evolution of Raman spectra as a function of regeneration time in figs. S10A and S11A (*17*) shows that isolated Mo oxide nanostructures were regenerated sequentially. Isolated $Mo(=O)_2$ species anchored on double Al-atom framework sites were regenerated first, as evidenced by a single initial Raman band at 993 cm^{-1}. With increased regeneration time, a second Raman band at 975 cm^{-1} caused by $Mo(=O)_2OH$ species anchored on single Al-atom sites appeared and grew in intensity. Finally, a third Raman band at 984 cm^{-1} due to $Mo(=O)_2$ species anchored on Si sites on the external surface of the zeolite appeared and grew in intensity for the catalyst with a lower Al concentration in the zeolite (Si/Al = 25 instead of 15). These direct spectroscopic observations demonstrate that exposure to gas-phase O_2 first regenerates isolated Mo oxide nanostructures anchored on sites with two Al atoms, then forces these species to migrate to sites with one Al atom and, eventually, to Si sites on the external surface of the zeolite.

A comparison of C_6H_6 formation rates in CH_4 conversion as a function of time on stream for a fresh 1.3 wt % Mo/ZSM-5 catalyst (Si/Al = 25) versus the same catalyst after deactivation in the reaction with CH_4 and subsequent regeneration for 120 min (Fig. 3A) demonstrates that the catalytic performance can be fully restored. The C_6H_6 formation rates after regeneration matched those for the fresh catalyst. Additional reaction results for C_6H_6 and H_2 formation rates for two 1.3 wt % Mo/ZSM-5 (Si/Al = 15 and 25) catalysts as a function of regeneration time (figs. S10 and S11) (*17*) show that both the overall activity and selectivity to C_6H_6 fully recovered after regeneration. Thus, rapid catalyst deactivation can be successfully addressed by regeneration with gas-phase O_2, and the catalyst lifetime can be extended by repeated regeneration cycles.

Correlations between the structure of the initial Mo oxide species and catalytic performance can be established by comparing the evolution of the Raman spectra with changes in reaction rates as a function of regeneration time in figs. S10 and S11 (*17*). The catalytic activity was restored once Mo oxide nanostructures on double Al-atom framework sites were regenerated (after ~20 min). With increased regeneration time, these isolated Mo oxide species migrated from double to single Al-atom zeolite framework sites, and the catalytic performance with CH_4 remained unchanged. Furthermore, the catalytic performance of a regenerated catalyst can be optimized and may exceed that of a fresh catalyst if the regeneration treatment is stopped before Mo oxide nanostructures are forced to migrate to Si anchoring sites on the external surface of the zeolite. Specifically for the 1.3 wt % Mo/ZSM-5 (Si/Al = 25) catalyst, Mo oxide nanostructures were regenerated and moved from double to single Al-atom zeolite framework sites for regeneration times between 20 and 100 min (fig. S11A) (*17*). Notably, Mo nanostructures remained anchored on zeolite framework Al sites when the regeneration was limited to this duration, and the rates of C_6H_6 formation for such regenerated catalyst samples actually exceeded those for the fresh catalyst. The C_6H_6 formation rates for a catalyst regenerated for 100 min in Fig. 3A exceeded those for the same catalyst before deactivation during the initial time on stream period. In contrast, when the regeneration time was extended beyond 100 min, Mo oxide nanostructures were forced to migrate from Al framework sites to Si anchoring sites on the external surface of the zeolite. This change in the anchoring sites caused the catalytic activity to decrease to the level of the fresh catalyst, and the C_6H_6 formation rates for the catalyst regenerated for 120 min (Fig. 3A) matched those for the fresh catalyst. With time on stream with CH_4, the catalytic activity declined likely because of migration, growth, and coking of Mo NPs, and the performance for all regenerated catalysts eventually became indistinguishable. However, in the first 60 min of time on stream, the benzene formation rates in Fig. 3A and fig. S11C (*17*) were dependent on the identity of the initial Mo oxide nanostructures.

For understanding these initial activity differences, transition-state DFT calculations were used for comparing CH_4 activation over catalytic Mo carbide nanostructures anchored on the identified three types of anchoring sites: double and single Al-atom zeolite framework sites and Si sites on the external surface of the zeolite. The calculations compared the first step (breaking of the CH_3-H bond in methane), which is likely the rate-determining step, over the Mo carbide nanostructure with a stoichiometry of Mo_4C_2 on the three zeolite anchoring sites (*29*). The CH_4 activation mechanism is similar for all anchoring sites, as illustrated in Fig. 3, which compares reaction pathways for a double Al-atom anchoring site inside a zeolite framework pore (Fig. 3, B, E, and F) and a Si site on the external surface of the

Table 1. DFT-calculated vibrational modes for isolated Mo oxide species supported on ZSM-5 (cm^{-1}): symmetric stretch (ν_s), asymmetric stretch (ν_{as}), and bend (δ).

Mo species	ν_s O=Mo=O	ν_{as} O=Mo=O	δ O=Mo=O
$Mo(=O)_2$ on a double Al-atom site	992	972	388
$Mo(=O)_2OH$ on a single Al-atom site	975	962	356

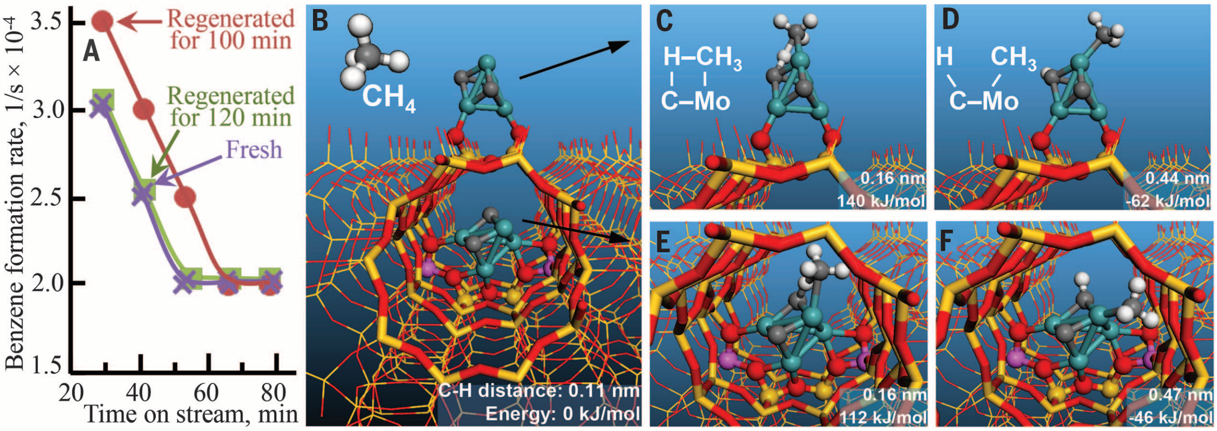

Fig. 3. Catalytic activity of Mo nanostructures. (**A**) Benzene formation rates in methane conversion over a 1.3 wt % Mo/ZSM-5 (Si/Al = 25) catalyst. The catalytic activity declines with time on stream but is fully restored after 120 min of gas-phase oxygen regeneration. Initial activity is enhanced by controlling the distribution of Mo nanostructures: Activity is higher after 100 min of regeneration when Mo oxide nanostructures are anchored mostly on framework Al sites and not forced to migrate to Si sites on the external surface of the zeolite. (**B** to **F**) Reaction mechanism calculations show that the energy barrier for methane activation with the formation of CH_3 and H species on the surface of the catalyst is lower when a Mo nanostructure is anchored on a framework Al site [(B), (E), and (F)] versus on a Si site on the external surface [(B) to (D)].

zeolite (Fig. 3, B to D). The CH$_4$ initially approaches an exposed Mo atom, an atom that is not directly bonded to the zeolite. In the transition state (Fig. 3, C and E), CH$_4$ forms a Mo-CH$_3$-H-C cycle in which the C atom of CH$_4$ binds to the exposed Mo atom and, simultaneously, one of the H atoms of CH$_4$ binds to a C atom in the carbide. Thus, a Mo-C pair of atoms in the Mo carbide nanostructure serves as a single catalytic active site. This dual Mo-C site activates CH$_4$ in a scissoring motion that produces a CH$_3$ group bonded to Mo and an H atom bonded to C of the carbide (Fig. 3, D and F). Although the mechanism of CH$_4$ activation is similar, differences in geometries and electronic properties of Mo carbide nanostructures anchored on Al and Si sites lead to differences in their catalytic properties. The CH$_4$ activation energy over the Mo carbide anchored on the double Al-atom site of 112 kJ/mol in Fig. 3E is lower than 140 kJ/mol for the Si site in Fig. 3C. The transition state for the single Al-atom anchoring site is analogous to that for the double Al-atom site in Fig. 3E, with a comparable activation energy of 117 kJ/mol (table S6) (*17*). The CH$_4$ reaction is therefore predicted to be dominated by the activity of Mo nanostructures anchored on framework Al sites. This computational result is consistent with known experimental observations that the catalytic activity of Mo nanostructures depends strongly on the Si/Al ratio of the supporting zeolite and declines substantially when Al framework sites are lost through dealumination (*2*, *8*, *13*–*15*, *30*).

The obtained information on the identity of Mo structures, their regeneration, and their influence on catalytic activity opens new opportunities for rational design of improved catalyst formulations and for optimizing reaction conditions for direct conversion of natural gas into liquid transportation fuels and valuable feedstocks for the chemical industry. It is important to control the distribution of Mo oxide species and limit their anchoring to framework Al sites because initial Mo oxide nanostructures anchored on Al sites of the zeolite framework are converting into carbided Mo NPs with higher catalytic activity than those produced by initial Mo oxide species anchored on Si sites. The number and distribution of single and double Al-atom anchoring sites can be optimized by adjusting a zeolite synthesis procedure. The number of Si anchoring sites on the external surface of the zeolite can be reduced, or these Si sites can be eliminated completely by adjusting the Mo deposition procedure. Furthermore, the catalytic performance of Mo species and their periodic regeneration can be optimized by adjusting catalyst formulations (for example, with promoter metals) and changing the temperatures of the reaction and regeneration, flow rates, and other reaction conditions.

REFERENCES AND NOTES

1. E. McFarland, *Science* **338**, 340–342 (2012).
2. J. H. Lunsford, *Catal. Today* **63**, 165–174 (2000).
3. S. G. Podkolzin, E. E. Stangland, M. E. Jones, E. Peringer, J. A. Lercher, *J. Am. Chem. Soc.* **129**, 2569–2576 (2007).
4. R. Khalilpour, I. A. Karimi, *Energy* **40**, 317–328 (2012).
5. International Energy Agency, "Golden rules for a golden age of gas - World Energy Outlook special report on unconventional gas," (International Energy Agency, Paris, France, 2012); www.worldenergyoutlook.org/goldenrules/.
6. J. A. Labinger, J. E. Bercaw, *Nature* **417**, 507–514 (2002).
7. X. Guo *et al.*, *Science* **344**, 616–619 (2014).
8. A. Holmen, *Catal. Today* **142**, 2–8 (2009).
9. L. Wang *et al.*, *Catal. Lett.* **21**, 35–41 (1993).
10. L. Y. Chen, L. W. Lin, Z. S. Xu, X. S. Li, T. Zhang, *J. Catal.* **157**, 190–200 (1995).
11. F. Solymosi, A. Erdöhelyi, A. Szöke, *Catal. Lett.* **32**, 43–53 (1995).
12. J. Z. Zhang, M. A. Long, R. F. Howe, *Catal. Today* **44**, 293–300 (1998).
13. Y. Xu, X. Bao, L. Lin, *J. Catal.* **216**, 386–395 (2003).
14. Z. R. Ismagilov, E. V. Matus, L. T. Tsikoza, *Energy Environ. Sci* **1**, 526–541 (2008).
15. T. V. Choudhary, E. Aksoylu, D. W. Goodman, *Catal. Rev. Sci. Eng.* **45**, 151–203 (2003).
16. J. J. Spivey, G. Hutchings, *Chem. Soc. Rev.* **43**, 792–803 (2014).
17. Supplementary materials are available on *Science* Online.
18. H. Tian, C. A. Roberts, I. E. Wachs, *J. Phys. Chem. C* **114**, 14110–14120 (2010).
19. E. L. Lee, I. E. Wachs, *J. Phys. Chem. C* **111**, 14410–14425 (2007).
20. E. L. Lee, I. E. Wachs, *J. Phys. Chem. C* **112**, 20418–20428 (2008).
21. S. Sklenak *et al.*, *Phys. Chem. Chem. Phys.* **11**, 1237–1247 (2009).
22. J. Dědeček, Z. Sobalík, B. Wichterlová, *Catal. Rev. Sci. Eng.* **54**, 135–223 (2012).
23. J.-P. Tessonnier *et al.*, *J. Phys. Chem. B* **110**, 10390–10395 (2006).
24. P. Hoffmann, J. A. Lobo, *Microporous Mesoporous Mater.* **106**, 122–128 (2007).
25. H. S. Lacheen, E. Iglesia, *J. Catal.* **230**, 173–185 (2005).
26. H. Aritani, H. Shibasaki, H. Orihara, A. Nakahira, *J. Environ. Sci. (China)* **21**, 736–740 (2009).
27. S. Liu, L. Wang, R. Ohnishi, M. Ichikawa, *J. Catal.* **181**, 175–188 (1999).
28. H. Zheng *et al.*, *J. Am. Chem. Soc.* **130**, 3722–3723 (2008).
29. J. Gao *et al.*, *J. Phys. Chem. C* **118**, 4670–4679 (2014).
30. J. P. Tessonnier, B. Louis, S. Rigolet, M. J. Ledoux, C. Pham-Huu, *Appl. Catal. A* **336**, 79–88 (2008).

ACKNOWLEDGMENTS

The work in S.G.P.'s group at Stevens Institute of Technology was supported by the NSF under grant CBET-1133987. The work in I.E.W.'s group at Lehigh University was supported by the NSF under grant CBET-1134012. The Materials Studio software was used under a collaborative research license from BIOVIA Corp. in San Diego, California. Author contributions: J.G. and Y.Z. obtained the computational and reaction-testing results and discussed the overall results; J.-M.J. and Y.T. obtained the experimental spectroscopic data and discussed the overall results; I.E.W. conceived and supervised the spectroscopic experiments and interpreted the results; and S.G.P. conceived and supervised the calculations and reaction testing, interpreted the results, and prepared the initial manuscript.

SUPPLEMENTARY MATERIALS

www.sciencemag.org/content/348/6235/686/suppl/DC1
Materials and Methods
Figs. S1 to S12
Tables S1 to S6
References
Movie S1

16 January 2015; accepted 26 March 2015
Published online 9 April 2015;
10.1126/science.aaa7048

INORGANIC CHEMISTRY

A synthetic Mn$_4$Ca-cluster mimicking the oxygen-evolving center of photosynthesis

Chunxi Zhang,[1]* Changhui Chen,[2] Hongxing Dong,[2]* Jian-Ren Shen,[3] Holger Dau,[4]* Jingquan Zhao[1]

Photosynthetic splitting of water into oxygen by plants, algae, and cyanobacteria is catalyzed by the oxygen-evolving center (OEC). Synthetic mimics of the OEC, which is composed of an asymmetric manganese-calcium-oxygen cluster bound to protein groups, may promote insight into the structural and chemical determinants of biological water oxidation and lead to development of superior catalysts for artificial photosynthesis. We synthesized a Mn$_4$Ca-cluster similar to the native OEC in both the metal-oxygen core and the binding protein groups. Like the native OEC, the synthetic cluster can undergo four redox transitions and shows two magnetic resonance signals assignable to redox and structural isomerism. Comparison with previously synthesized Mn$_3$CaO$_4$-cubane clusters suggests that the fourth Mn ion determines redox potentials and magnetic properties of the native OEC.

The oxygen-evolving center (OEC) in photosystem II (PSII) of plants, algae, and cyanobacteria facilitates splitting of water into O$_2$, protons, and electrons (*1*–*4*). Crystallographic structures (*5*–*8*) reveal that the core of the OEC consists of a Mn$_3$CaO$_4$ cubane motif and a "dangler" Mn linked via two bridging oxides, forming a distinct asymmetric Mn$_4$Ca-cluster (Fig. 1A). This cluster is coordinated to four water molecules, one imidazole, and six carboxylate groups of the amino acid residues of the PSII polypeptides (Fig. 1C). The structure of the OEC as well as the oxidation states of the four manganese ions undergo changes during the water-oxidation reaction cycle, or S-state cycle (*4*, *9*, *10*). Spectroscopic results and computational chemistry have provided insight in reaction intermediates and mechanisms (*4*, *9*–*16*). The lability of

Identification of molybdenum oxide nanostructures on zeolites for natural gas conversion

Jie Gao *et al.*

Science **348**, 686 (2015);
DOI: 10.1126/science.aaa7048

This copy is for your personal, non-commercial use only.

If you wish to distribute this article to others, you can order high-quality copies for your colleagues, clients, or customers by clicking here.

Permission to republish or repurpose articles or portions of articles can be obtained by following the guidelines here.

The following resources related to this article are available online at www.sciencemag.org (this information is current as of August 30, 2015):

Updated information and services, including high-resolution figures, can be found in the online version of this article at:
http://www.sciencemag.org/content/348/6235/686.full.html

Supporting Online Material can be found at:
http://www.sciencemag.org/content/suppl/2015/04/08/science.aaa7048.DC1.html

This article **cites 28 articles**, 2 of which can be accessed free:
http://www.sciencemag.org/content/348/6235/686.full.html#ref-list-1

This article appears in the following **subject collections:**
Chemistry
http://www.sciencemag.org/cgi/collection/chemistry

Downloaded from www.sciencemag.org on August 30, 2015

Science (print ISSN 0036-8075; online ISSN 1095-9203) is published weekly, except the last week in December, by the American Association for the Advancement of Science, 1200 New York Avenue NW, Washington, DC 20005. Copyright 2015 by the American Association for the Advancement of Science; all rights reserved. The title *Science* is a registered trademark of AAAS.